Cloud-Resolving ICON Simulations of Secondary Ice Production in Arctic Mixed-Phase Stratocumuli Observed during M-PACE

A. Possner, K. Pfannkuch, V. Ramadoss

Institute for Atmospheric and Environmental Sciences, Goethe University Frankfurt, Frankfurt, Germany

Corresponding author: Anna Possner, apossner@iau.uni-frankfurt.de

ABSTRACT: This document provides background information to the presentation given at EGU. It includes a wider placement of this study in the current literature and detailed information on the applied modeling strategy

1. Motivation

Boundary layer mixed-phase clouds (MPCs) impact Earth's energy balance during boreal winter in the mid-latitudes and the Arctic, and all-year around in austral mid-latitudes (Korolev et al. 2017). While MPCs contain a mixture of liquid and ice, their radiative impact is governed by their liquid-phase properties in optically thick MPCs. However, these may be altered by the formation and growth of ice-phase hydrometeors through the depletion of cloud liquid by the Wegener-Bergeron-Findeisen (WBF) process (Wegener 1911; Bergeron 1935; Findeisen 1938) and riming (Lasher-Trapp et al. 2021; Tornow et al. 2021). The interactions between the ice and liquid phase in MPCs are extremely complex and remain insufficiently constrained from observations. In general though we know the total sink on cloud condensate to be strongly dependent on the ice crystal number concentration (n_i) generated in the cloud (e.g. Vergara-Temprado et al. (2018)). These ice crystals can form via primary nucleation on available ice nucleating particles (INPs) or secondary ice production (SIP). We know that primary nucleation in boundary layer MPCs is governed by immersion freezing (Murray et al. 2012). Meanwhile, contributions from SIP remain poorly constrained due to our still incomplete understanding of the involved mechanisms. In general, SIP refers to the generation of an ice crystal without the presence of an INP. Seven potential SIP mechanisms have been identified and studied in laboratory experiments and their contributions are likely cloud regime dependent (Field et al. 2017; Korolev and Leisner 2020). Most climate models merely consider contributions from the longest known rime-splintering mechanism by Hallet-Mossop (Hallet and Mossop 1974; Mossop and Hallett 1974). However, it is unlikely to be effective in moderately supercooled mixed-phase stratocumuli due to its limited temperature range. Fragmentation of millimeter-sized rain drops upon freezing (Lauber et al. 2018) has been shown to dominate SIP in convective clouds with relatively warm cloud bases (Sullivan et al. 2018). However, it has not been shown to contribute to SIP in Arctic stratiform clouds (Fu et al. 2019; Sotiropoulou et al. 2020). Other SIP mechanisms related to drop evaporation have also been shown to be ineffective in Arctic mixed-phase stratocumuli (Fridlind et al. 2007).

Meanwhile, field measurements indicate that droplet shattering (DS, Luke et al. (2021); Pasquier et al. (2022)) or the fragmentation due to collisional breakup (BR, Rangno and Hobbs (2001); Schwarzenboeck et al. (2009)) may contribute to SIP in Arctic low-level clouds. Numerical

sensitivity studies of either mechanism in mixed-phase stratocumuli have shown that BR is seemingly more effective in warmer supercooled temperature ranges (Sotiropoulou et al. 2020, 2021b) and DS in colder (T¡−10°C) clouds (Sotiropoulou et al. 2020; Zhao et al. 2021). However, many uncertainties remain with respect to the assumptions made within these parameterizations which may alter their efficacy and thus the impact of either mechanism on cloud evolution.

In this study we investigate the impact of BR and DS on cloud evolution in cloud-resolving simulations performed with the Icosahedral Nonhydrostatic Weather and Climate (ICON) model (Dipankar et al. 2015) for a case of single-layer supercooled stratocumuli observed during the Mixed-Phase Arctic Cloud Experiment (M-PACE, Verlinde et al. (2007)). The intention of this work is three-fold. Firstly, we wish to assess the efficacy of either process in a well established case of moderately supercooled Arctic MPCs in ICON. While, ICON has been shown to adequately capture Arctic MPC fields at the cloud-resolving scale (Schemann and Ebell 2020), it has not yet been evaluated with respect to SIP in this regime. Secondly, we wish to explore the importance of complexity of primary freezing paramaterizations in a cloud regime where n_i is seemingly dominated by SIP. And thirdly, to enhance our understanding of either SIP mechanism in simulations with resolved cloud-generated boundary-layer dynamics.

2. Model and Parameterizations

a. ICON Model

We use idealized ICON-LEM (large eddy mode) simulations in this study. The triangular grid of ICON is projected on a torus, which renders the implementation of periodic boundary conditions obsolete. The non-hydrostatic and fully compressible Navier Stokes equations are solved using C-type staggering (Zängl et al. 2015). An explicit two-time level predictor-corrector scheme is used for time integration, which treats the vertical propagation of sound waves implicitly (Dipankar et al. 2015). Furthermore, Rayleigh damping following the method of Klemp et al. (2008) is applied (Heinze et al. 2017).

The implicit treatment of sound waves requires the simulations to be run with a small time step. A basic time step (dt) is used for tracer transport, numerical diffusion and fast-physics parameterizations. A sub-time stepping is applied for the dynamical core. Slow physics (i.e. radiation) is

computed on a longer time step specified as a multiple of the basic time step (Heinze et al. 2017). Radiative fluxes are computed using ecRad (Hogan and Bozzo 2018), which was developed at the "European Centre for Medium-Range Weather Forecast" (ECMWF) and implemented in ICON. Subgrid-scale turbulence is parameterized using a Smagorinsky scheme (Dipankar et al. 2015).

The cloud microphysics is parameterized with the Seifert and Beheng (2006) two-moment bulk microphysics scheme. The activation of cloud droplets is calculated explicitly (Hande et al. 2016) using fits best capturing the dependence of CCN concentrations on vertical velocity at different pressure levels under European conditions. Beydoun and Hoose (2019) introduced a simple scaling factor to these fits to represent CCN concentrations at different geographical locations. For the clean conditions sampled during M-PACE (CCN concentrations between $23\,\mathrm{cm}^{-3}$ and $73\,\mathrm{cm}^{-3}$) a scaling factor of 0.05 was specified.

The standard implementation of the (Seifert and Beheng 2006) microphysics scheme can be executed either with prescribed INP concentrations, or using a simplified spatio-temporally varying implementation of INP. In both cases INP concentrations are specified for the low troposphere and drop off exponentially with altitude. The latter implementation requires the simulation to be run with two additional tracers, which are advected with the flow. One tracer stores the background concentration of INP and the other the activated fraction (in_{act}). In regions sub-saturated with respect to ice, the activated fraction is relaxed back to zero over a characteristic prescribed timescale τ_{relax} (Equ. 1).

$$in_{act} = in_{act}\left(1 - \frac{dt}{\tau_{relax}}\right) \tag{1}$$

In cases with significant surface precipitation (frozen), the background INP concentration will be depleted in the absence of an INP source. During M-PACE surface precipitation rates remained below 1 mm per day. There is no significant increase in computation time associated with the addition of these two tracers.

b. Prognostic Representation of Primary Nucleation

In addition to the characteristic time-scale formulation associated with INP cycling, we assess the impact of SIP in simulations with a full prognostic treatment of INP with simplified aerosol. This

formulation follows the approach suggested by Solomon et al. (2015), which uses the following budget equation for INP concentrations:

$$\frac{\partial INP}{\partial dt} = ADV + DIFF + \left.\frac{\partial INP}{\partial dt}\right|_{nuc} + \left.\frac{\partial INP}{\partial dt}\right|_{subl.} \tag{2}$$

where ADV and $DIFF$ refer to the rates of change in INP due to advection and turbulent diffusion. The nucleation term represents the loss of INP through nucleation (in this case immersion freezing) and the sublimation term refers to the INP replenished by fully sublimating ice crystals. Using this approach, Solomon et al. (2015) demonstrated the importance of INP recycling for the maintenance of Arctic MPCs governed by primary nucleation.

The INP concentrations are initialized following the empirical fit of DeMott et al. (2015):

$$INP(T) = cN_a^{(\alpha(273.16-T)+\beta)} \times e^{(\gamma(273.16-T)+\delta)} \tag{3}$$

Here, N_a describes the number of aerosol particles with diameters larger than $0.5\,\mu$m per cm^{-3} and T denotes the temperature in Kelvin. The other constant parameters have the following values: $c = 10^3$, $\alpha = 0.0$, $\beta = 1.25$, $\gamma = 0.46$ and $\delta = -11.6$. This curve is discredited into 15 temperature bins. Thus each bin holds the amount of potential INP within a certain temperature range at each location and each point in time. Thus this scheme adds 15 tracers to the computation. The initialization of this scheme for M-PACE is specified in section 2b.

The INP will be removed from each bin during immersion freezing events when $lwc > 10^{-3}$ gkg^{-1} and the atmospheric temperature is at, or below, the temperature of each of the 15 bins considered. When ice crystals (or snow and graupel) with immersed INP sublimate, these INP are once again released and may freeze again if re-entrained into the liquid cloud layer. This source term of INPs is implemented in proportion to the amount of depletion occurring within each bin due to immersion freezing using weighting functions:

$$w_{k,t} = \frac{\widetilde{INP}(k,0) - \widetilde{INP}(k,t)}{\widetilde{INP}(k,0)} \tag{4}$$

for each temperature bin k at time t. These weights $w_{k,t}$ are normalized such that $\sum_{k=1}^{15} w_{k,t} = 1 \forall t$. $\widetilde{INP(k,t)}$ describes the accumulated total number of INP at temperature bin k in the entire

simulation domain at time t. Upon sublimation, INP in each temperature bin k are released in proportion to $w_{k,t}$, and the temporally varying bulk INP number concentration contained at each grid point in all frozen hydrometeor species. For this accounting three INP tracers for ice, snow, and graupel respectively were implemented in addition to the 15 temperature-bin INP tracers. In cases where SIP is active, n_i may be dominated by SIP (section **??**). We thus need to track primary and secondary ice, snow, and graupel hydrometeors in order to prevent the artificial generation of INP through sublimating secondary hydrometeors. This is further described in more detail in section 2e. Overall, the computational cost is approximately tripled when a prognostic INP budget is considered in the presence of SIP.

c. Implementation of Droplet Shattering

The Phillips et al. (2018) parameterization for DS is implemented in ICON. The empirical scheme considers two types of collisions: (i) collisions between rain drops and smaller ice crystals or snow flakes, and (ii) collisions between rain drops and larger snow flakes, or graupel. For the first type of collisions an empirical formula is fitted against laboratory data in the temperature range from -4 to -25° C and for rain drop sizes between 0.06 to 1.6 mm. Furthermore, either "big" fragments or "tiny" splinters may be generated by the shattering rain drop. This is included in the parameterization in terms of two separate functional fits for the total number of generated fragments (n_t) and the number of ejected large fragments (n_b) per collision. Further details regarding the functional form, accuracy of the fit and used laboratory observations are provided in Phillips et al. (2018). The basic structure of the empirical formula describing $n_{t,1}$ and n_b is repeated here:

$$n_{t,1} = \Xi(D)\Omega(D)\left[\frac{\zeta\eta^2}{(T-T_0)^2+\eta^2}+\beta T\right] \qquad \forall m > m_f \tag{5}$$

$$n_b = min\left\{\Xi(D)\Omega(D)\left[\frac{\zeta_b\eta_b^2}{(T-T_{b,0})^2+\eta_b^2}\right], n_{t,1}\right\} \tag{6}$$

where T denotes the temperature in °C, D and m the diameter and mass of the rain drop respectively, and m_f the mass of the colliding frozen ice or snow crystal. Ξ and Ω denote threshold functions for the onset of fragmentation through DS in terms of size and temperature, and η, η_b, ζ, ζ_b, T_0, and $T_{b,0}$ are derived by the fit. The mass of the fragments is calculated assuming $m_{t,1} = \rho_i \pi D_t^3/6$

with $\rho_i = 920\,\mathrm{kgm}^{-3}$ and $D_{t,1} = 10\,\mu$m. Big splinters are added to the graupel category and small splinters to the ice category.

For collisions of the second kind, the formulation for the number of ejected particles per collision ($n_{t,2}$) is proportional to the ratio (r_e) of available kinetic energy of the collision (e_k) to the surface energy:

$$n_{t,2} = 3\Phi(T) \times [1 - f(T)] \times max\{r_e - r_{e,c}, 0\} \qquad \forall m > m_f \text{ and } D > 150\,\mu\,\mathrm{m} \tag{7}$$

where f(T) denotes the frozen fraction and $\Phi(T)$ is a function of the frozen fraction and the required minimum energy ratio $r_{e,c}$ is prescribed as 0.2. All ejected crystals are assumed to be of the same mass, which is specified as $m_{t,2} = 0.001m$.

d. Implementation of Collisional Breakup

A parameterization based on energy conservation during collisions proposed by Phillips et al. (2017) is implemented. This parameterization computes the number of ejected particles per ice-ice collision (n_{br}) as a function of e_k, the surface area of the smaller colliding particle α multiplied by the asperity surface density A:

$$n_{br} = \alpha A \left(1 - \exp\left(-\left(\frac{C e_k}{\alpha A}\right)^{\gamma}\right)\right) \tag{8}$$

The argument of the exponential function denotes the ratio between e_k and the work required to break off asperities in the region of contact. C denotes the asperity-fragility coefficient which is prescribed as 10815 for dendrites and 24780 for spatial planar crystals. The final parameter γ is related to the riming intensity of the crystal as $\gamma = 0.5 - 0.25RF$, where RF denotes the rimed fraction.

A is primarily determined by crystal habit, size and RF of the smaller colliding particle. It is thus indirectly a function of T and supersaturation with respect to ice, which determines the habit and growth history of the shattering ice crystal. The scheme considers ice-ice, ice-snow, snow-snow, ice-graupel, snow-graupel and graupel-graupel collisions. Different expressions for A and C are used depending on the hydrometeor type of the smaller colliding particle (see Table 1

of Phillips et al. (2017)). Finally, all generated fragments are initialized with 0.1 % of the mass of the colliding particles and are transferred to the ice category.

e. Treatment of Primary and Secondary Ice

The implementation of a prognostic INP budget (section2b) under active SIP conditions, requires a separate tracing of primary and secondary ice in order to prevent artificial INP generation. Fig. 2 in Zhao et al. (2021) shows that in the simulated temperature range during M-PACE up to a 100 fragments per collision may be generated. Thus, not tracing INP, and thus primary ice until sublimation, may artificially increase background INP concentrations by several orders of magnitude over time.

Thus in addition to the 10 tracers carrying the information of mass and number concentration of the 5 hydrometeor species (cloud, rain, ice, snow, and graupel), 6 new additional tracers were implemented for the mass and number concentration of secondary ice, snow and graupel (virtually non-existent in our simulations, but implemented for completeness). Hydrometeors described by these modes do not contain INP, but otherwise undergo the exact same processes as primary ice, snow and graupel. The mass and number concentration of primary ice and snow is stored in 6 additional primary ice-hydrometeor tracers. Both, primary and secondary tracers are combined in the hydrometeor tracers for all ice, snow and graupel which enter the radiation scheme.

The purpose of these 12 new tracers is to distinguish crystals containing (at last one) INP, or none. Thus following aggregation between colliding primary and secondary frozen hydrometeors, the resulting aggregate is shifted into the primary category. Furthermore, while no mass transfer is initiated originally by BR through primary ice with primary ice collisions, the resulting splinters are shifted into the secondary ice category and removed from the primary ice budget. This accounting is also performed for DS if the shattering is triggered by collisions through primary frozen hydrometeors and rain drops.

3. Observations and Simulation Setup

a. M-PACE Case and Observations

Our case study focuses on the single-layer cloud deck sampled during the Mixed-Phase Arctic Cloud experiment (M-PACE) between October 9^{th} – 10^{th} 2004 (Verlinde et al. 2007) along the North Slope of Alaska. During this time a strong capping inversion (Fig. 1a) formed under a persistent high pressure system. Meanwhile cloud formation was governed by strong sensible and latent surface heat fluxes (136.5 W m^{-2} and 107.7 W m^{-2} respectively) from the ice-free ocean surface. Cloud-top temperatures around -17°C were observed, which are well outside the Hallet-Mossop temperature range, which makes this a suitable case to study the impact of other SIP mechanisms within persistent single-layer stratocumuli.

The soundings shown in Fig. 1a and Fig. 1b are available from the Atmospheric Radiation Measurement (ARM) station at Utqiaġvik. Profiles of liquid water content (lwc, Fig. 1c) and ice water content (iwc, Fig. 1d) are obtained from the "Continuous Baseline Microphysical" (MICROBASE) retrieval product. These value-added baseline retrievals of cloud properties are obtained from a combination of the 35-GHz millimeter wavelength cloud radar, micropulse lidar, and microwave radiometer (compiled by S. Giangrande and M. Jensen 2002). Peak values of iwc reach around 6 % of the observed peak in lwc. Estimates (Shupe et al. 2006; Turner et al. 2007) of vertical integrated quantities, i.e. liquid (lwp) and total ice ($tiwp$) water paths, were also based on the combined lidar/radar retrievals at Utqiaġvik and Oliktok point, and are provided as $lwp = 160 \pm 50$ gm^{-2} and $tiwp = 15 \pm$ a factor of two (i.e. the ice water path could be between 8 and 30 gm $^{-2}$).

In-situ measurements of droplet number concentration (n_d) and n_i from three stair-case research flights performed between Utqiaġvik and Oliktok point are available. McFarquhar et al. (2007) inferred n_d from the forward scattering spectrometer probe (FSSP) which measures particle diameters between 3 and 53 μm providing 10 s running averages. Meanwhile, n_i is inferred from a combination of different cloud probes measuring at different size ranges. This includes the one- and two-dimensional cloud probes, which measure in size ranges between 20 and 620 μm, and 30 and 960 μm, and the high-volume precipitation sampler, which measures particles between 0.4 and 40 mm. Within the mixed-phase regime, which is identified using the Rosemount Icing Detector, particles larger than 53 μm are considered as ice in the absence of drizzle.

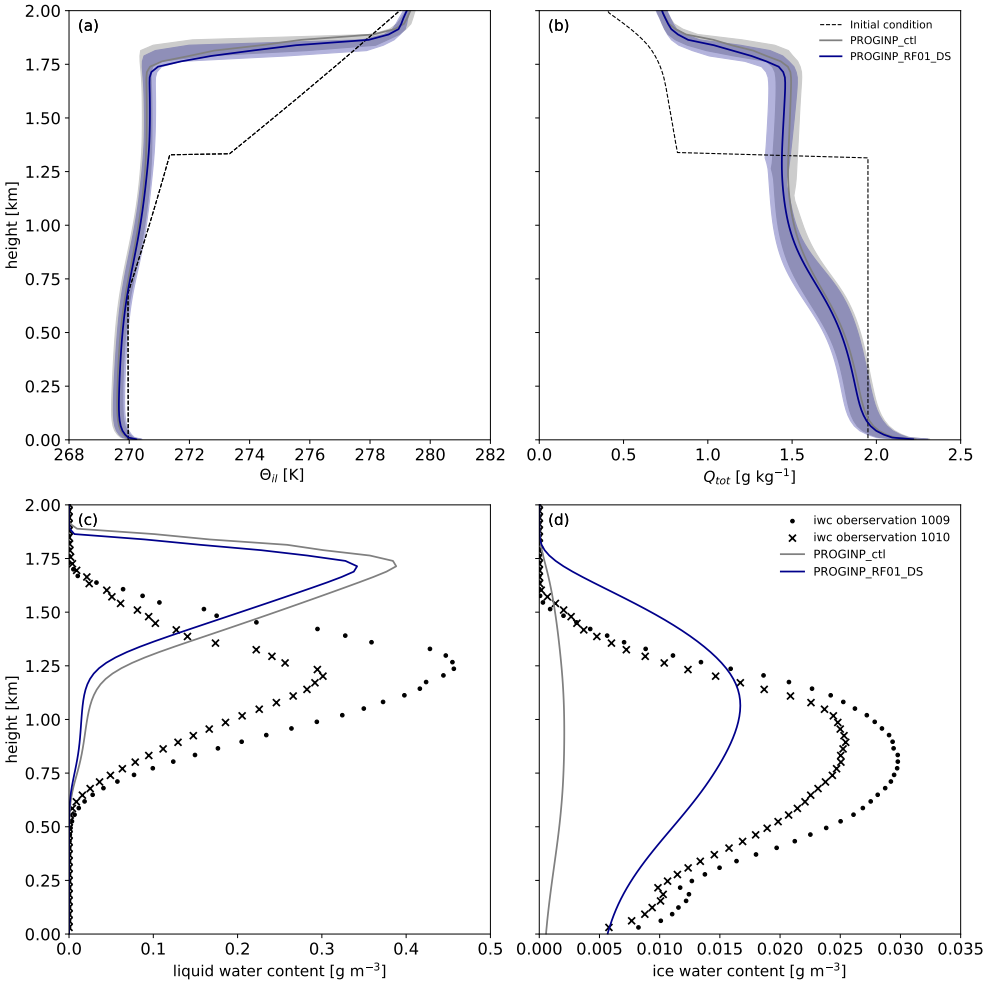

FIG. 1. Soundings of a) ice-liquid potential temperature and b) total water content Q_{tot} (including ice crystal mass contribution), in comparison to simulated thermodynamic profiles for two sensitivity experiments defined in table 1. Remote sensing estimates for c) liquid water content (lwc) and d) total ice water content (iwc).

N_i measurements obtained during M-PACE are still susceptible to artificial shattering at the inlet of the cloud probes, which is mitigated by anti-shattering coatings on tips used in later field campaigns. Several studies estimate that this can artificially increase measured n_i by a factor $2-5$ (e.g. Field et al. (2003); Febvre et al. (2012)), and in some data samples up to a factor 10 (Korolev et al. 2011), though many of these fragments are likely to be smaller than the required minimum diameter of 53 μm (Febvre et al. 2012) for the n_i estimate. Nonetheless, all ice crystal measurements with diameters less than 500 μm are prone to biases by inlet shattering. Thus a correction factor of 0.25 is applied as suggested by Jackson and McFarquhar (2014) and Jackson et al. (2014) to n_i

TABLE 1. Summary of sensitivity experiments. Experiments differ by the specified INP treatment, the inclusion of BR and RF assumptions made within the BR scheme, as well as the inclusion of DS.

Simulation	INP	DS	CB	RF
PROGINP_ctl	prognostic	off	off	–
PROGINP_RF02		off	on	0.2
PROGINP_RF03		off	on	0.3
PROGINP_RF04		off	on	0.4
PROGINP_DS		on	off	–
PROGINP_RF01_DS		on	on	0.2
PROGINP_RF02_DS		on	on	0.3
PROGINP_noPRIM	no immersion freezing after 10 h	on	on	0.1
PROGINP_10INP	prognostic w 10xINP	off	off	–
RELINP_DS		on	off	–
RELINP_RF01_DS		on	on	0.1
RELINP_RF02_DS		on	on	0.2

measurements from McFarquhar et al. (2007).

b. Simulation Setup

The cloud-resolving simulations are performed on a $25 \times 22\,\mathrm{km}^2$ domain with an edge length (= length of one side of equilateral triangle) of 125 m. The simulations are run for a 24 h period with a time step of 1 s. The slow time step (for the radiation scheme) is set to 10 min. All simulations are performed with 144 vertical levels and a domain top of 23 km. In the lowest 2.1 km of the atmosphere a vertical resolution of 25 m is prescribed. Above this threshold the vertical resolution decreases with height. Rayleigh damping is applied from an altitude of 3 km onward.

The simulations are initialized with the 17 UTC sounding obtained at Utqiaġvik on October 9^{th} 2004. The large-scale forcing for subsidence and the horizontal advection of moisture and heat are based on ECMWF analysis fields and are prescribed as in Klein et al. (2009). The simulations are performed with a fixed sea-surface temperature of 0.86° C and interactive surface fluxes.

Two different types of experiments are performed using either a prognostic budget implementation for INP (section 2b), or a computationally more efficient approach characterized by τ_{relax}

(section 2a). These will be referred to as $PROGINP$ and $RELINP$ experiments from hereon. During M-PACE a mean INP concentration of $0.16\,l^{-1}$ was measured (Prenni et al. 2007). Thus N_a was specified as $5.5\,cm^{-3}$, such that on average the sum across all temperature bins available for nucleation at a given cloud top temperature equals the observed INP concentration. This rescaling was necessary as lower cloud top temperatures were simulated than observed (due to an upward shift in the inversion height). For the vertical average only INP between 500 m and cloud top were considered as the aircraft only measured INP concentrations in that range. The warmest temperature bin contains all available INP down to a temperature of $-9.8\,°C$, whereas the bin width of the subsequent 14 bins were specified as $0.7\,°C$.

To provide comparable INP conditions, the immersion freezing of the $RELINP$ was adjusted such that the background INP are also calculated consistent with equ. 3 using similar parameter specifications as in $PROGINP$.

The default BR parameterization considers a temperature dependent habit classification of dendrites between -12°C to -17°C and spatial planar between -9°C to -12°C and -17°C to -40°C. As this formulation introduces an instantaneous habit change throughout the simulated cloud profile during M-PACE (Fig. 1a), we run the simulations with a fixed habit categorization of spatial planar, which qualitatively is consistent with Cloud Particle Imager images, though large amounts of spherical ice were also observed in the upper half of the cloud (McFarquhar et al. 2007).

The $PROGINP$ experiments contain six new hydrometeor species for secondary ice (section 2e). This allows us to track activated INP and to quantify the relative mass and number fractions of primary versus secondary ice at any given grid point throughout the simulation. Different experiments are conducted considering both SIP mechanisms in isolation or conjunction. Several studies (Sotiropoulou et al. 2020, 2021a,b) have shown BR to be governed by assumptions in RF, which remains unconstrained from observations. We thus include sensitivity experiments with RF ranging between 0.1 and 0.4. All numerical experiments are summarized in Table 1.

References

Bergeron, T., 1935: *On the physics of clouds and precipitation*. in *Proces Verbaux de l'Association de Mètèorologie, 5th asssembly of the International Union of geodesy and geophysics* ed., Paul Dupont, Paris, France, 156–178 pp.

Beydoun, H., and C. Hoose, 2019: Aerosol-cloud-precipitation interactions in the context of convective self-aggregation. *Journal of Advances in Modeling Earth Systems*, **11 (4)**, 1066–1087, https://doi.org/https://doi.org/10.1029/2018MS001523, URL https://agupubs.onlinelibrary.wiley.com/doi/abs/10.1029/2018MS001523, https://agupubs.onlinelibrary.wiley.com/doi/pdf/10.1029/2018MS001523.

compiled by S. Giangrande and M. Jensen, 2002: *Continuous Baseline Microphysical Retrieval (MICROBASEPI2)*. https://doi.org/10.5439/1034923, Atmospheric Radiation Measurement (ARM) user facility. Data set accessed [2022-08-22].

DeMott, P. J., and Coauthors, 2015: Integrating laboratory and field data to quantify the immersion freezing ice nucleation activity of mineral dust particles. *Atmos. Chem. Phys.*, **15**, 393–409, https://doi.org/10.5194/acp-15-393-2015.

Dipankar, A., B. Stevens, R. Heinze, C. Moseley, G. Zängl, M. Giorgetta, and S. Brdar, 2015: Large eddy simulation using the general circulation model icon. *Journal of Advances in Modeling Earth Systems*, **7 (3)**, 963–986, https://doi.org/https://doi.org/10.1002/2015MS000431, URL https://agupubs.onlinelibrary.wiley.com/doi/abs/10.1002/2015MS000431, https://agupubs.onlinelibrary.wiley.com/doi/pdf/10.1002/2015MS000431.

Febvre, G., J.-F. Gayet, V. Shcherbakov, C. Gourbeyre, and O. Jourdan, 2012: Some effects of ice crystals on the fssp measurements in mixed phase clouds. *Atmospheric Chemistry and Physics*, **12 (19)**, 8963–8977, https://doi.org/10.5194/acp-12-8963-2012, URL https://acp.copernicus.org/articles/12/8963/2012/.

Field, P. R., R. Wood, P. R. A. Brown, P. H. Kaye, E. Hirst, R. Greenaway, and J. A. Smith, 2003: Ice particle interarrival times measured with a fast fssp. *Journal of Atmospheric and Oceanic Technology*, **20 (2)**, 249 – 261, https://doi.org/10.1175/1520-0426(2003)020⟨0249:IPITMW⟩2.

0.CO;2, URL https://journals.ametsoc.org/view/journals/atot/20/2/1520-0426_2003_020_0249_ipitmw_2_0_co_2.xml.

Field, P. R., and Coauthors, 2017: Secondary ice production: Current state of the science and recommendations for the future. *Meteorological Monographs*, **58**, 7.1 – 7.20, https://doi.org/10.1175/AMSMONOGRAPHS-D-16-0014.1, URL https://journals.ametsoc.org/view/journals/amsm/58/1/amsmonographs-d-16-0014.1.xml.

Findeisen, W., 1938: Kolloid-meteorologische vorgänge bei niederschlagsbildung. *Meteorol. Z.*, **55**, 121–133.

Fridlind, A. M., A. S. Ackerman, G. McFarquhar, G. Zhang, M. R. Poellot, P. J. DeMott, A. J. Prenni, and A. J. Heymsfield, 2007: Ice properties of single-layer stratocumulus during the Mixed-Phase Arctic Cloud Experiment: 2. model results. *J. Geophys. Res.*, **112 (D24202)**, https://doi.org/10.1029/2007/JD008646.

Fu, S., X. Deng, M. D. Shupe, and H. Xue, 2019: A modelling study of the continuous ice formation in an autumnal arctic mixed-phase cloud case. *Atmospheric Research*, **228**, 77–85, https://doi.org/https://doi.org/10.1016/j.atmosres.2019.05.021, URL https://www.sciencedirect.com/science/article/pii/S0169809518313905.

Hallet, J., and S. Mossop, 1974: Production of secondary ice particles during the riming process. *Nature*, **(249)**, 26–28, https://doi.org/10.1038/249026a0.

Hande, L. B., C. Engler, C. Hoose, and I. Tegen, 2016: Parameterizing cloud condensation nuclei concentrations during hope. *Atmospheric Chemistry and Physics*, **16 (18)**, 12 059–12 079, https://doi.org/10.5194/acp-16-12059-2016, URL https://acp.copernicus.org/articles/16/12059/2016/.

Heinze, R., and Coauthors, 2017: Large-eddy simulations over germany using icon: a comprehensive evaluation. *Quarterly Journal of the Royal Meteorological Society*, **143 (702)**, 69–100, https://doi.org/https://doi.org/10.1002/qj.2947, URL https://rmets.onlinelibrary.wiley.com/doi/abs/10.1002/qj.2947, https://rmets.onlinelibrary.wiley.com/doi/pdf/10.1002/qj.2947.

Hogan, R. J., and A. Bozzo, 2018: A flexible and efficient radiation scheme for the ecmwf model. *Journal of Advances in Modeling Earth Systems*, **10 (8)**, 1990–2008, https://doi.org/https://doi.

org/10.1029/2018MS001364, URL https://agupubs.onlinelibrary.wiley.com/doi/abs/10.1029/2018MS001364, https://agupubs.onlinelibrary.wiley.com/doi/pdf/10.1029/2018MS001364.

Jackson, R. C., and G. M. McFarquhar, 2014: An assessment of the impact of antishattering tips and artifact removal techniques on bulk cloud ice microphysical and optical properties measured by the 2d cloud probe. *Journal of Atmospheric and Oceanic Technology*, **31 (10)**, 2131 – 2144, https://doi.org/https://doi.org/10.1175/JTECH-D-14-00018.1, URL https://journals.ametsoc.org/view/journals/atot/31/10/jtech-d-14-00018_1.xml.

Jackson, R. C., G. M. McFarquhar, J. Stith, M. Beals, R. A. Shaw, J. Jensen, J. Fugal, and A. Korolev, 2014: An assessment of the impact of antishattering tips and artifact removal techniques on cloud ice size distributions measured by the 2d cloud probe. *Journal of Atmospheric and Oceanic Technology*, **31 (12)**, 2567 – 2590, https://doi.org/https://doi.org/10.1175/JTECH-D-13-00239.1, URL https://journals.ametsoc.org/view/journals/atot/31/12/jtech-d-13-00239_1.xml.

Klein, S. A., and Coauthors, 2009: Intercomparison of model simulations of mixed-phase clouds observed during the ARM Mixed-Phase Arctic Cloud Experiment. I: single-layer cloud. *Q. J. R. Meteorol. Soc.*, **135**, 979–1002, https://doi.org/10.1002/qf.416.

Klemp, J. B., J. Dudhia, and A. D. Hassiotis, 2008: An upper gravity-wave absorbing layer for nwp applications. *Monthly Weather Review*, **136 (10)**, 3987 – 4004, https://doi.org/10.1175/2008MWR2596.1, URL https://journals.ametsoc.org/view/journals/mwre/136/10/2008mwr2596.1.xml.

Korolev, A., and T. Leisner, 2020: Review of experimental studies of secondary ice production. *Atmospheric Chemistry and Physics*, **20 (20)**, 11 767–11 797, https://doi.org/10.5194/acp-20-11767-2020, URL https://acp.copernicus.org/articles/20/11767/2020/.

Korolev, A., and Coauthors, 2017: Mixed-Phase Clouds: Progress and Challenges. *Meteorological Monographs*, **58**, 5.1–5.50, https://doi.org/10.1175/AMSMONOGRAPHS-D-17-0001.1.

Korolev, A. V., E. F. Emery, J. W. Strapp, S. G. Cober, G. A. Isaac, M. Wasey, and D. Marcotte, 2011: Small ice particles in tropospheric clouds: Fact or artifact? airborne icing instrumentation evaluation experiment. *Bulletin of the American Meteorological Society*, **92 (8)**,

967 – 973, https://doi.org/10.1175/2010BAMS3141.1, URL https://journals.ametsoc.org/view/journals/bams/92/8/2010bams3141_1.xml.

Lasher-Trapp, S., E. L. Scott, E. Järvinen, M. Schnaiter, F. Waitz, P. J. DeMott, C. S. McCluskey, and T. C. J. Hill, 2021: Observations and modeling of rime splintering in southern ocean cumuli. *Journal of Geophysical Research: Atmospheres*, **126 (23)**, e2021JD035 479, https://doi.org/https://doi.org/10.1029/2021JD035479, URL https://agupubs.onlinelibrary.wiley.com/doi/abs/10.1029/2021JD035479, e2021JD035479 2021JD035479, https://agupubs.onlinelibrary.wiley.com/doi/pdf/10.1029/2021JD035479.

Lauber, A., A. Kiselev, T. Pander, P. Handmann, and T. Leisner, 2018: Secondary ice formation during freezing of levitated droplets. *Journal of the Atmospheric Sciences*, **75 (8)**, 2815 – 2826, https://doi.org/10.1175/JAS-D-18-0052.1, URL https://journals.ametsoc.org/view/journals/atsc/75/8/jas-d-18-0052.1.xml.

Luke, E. P., F. Yang, P. Kollias, A. M. Vogelmann, and M. Maahn, 2021: New insights into ice multiplication using remote-sensing observations of slightly supercooled mixed-phase clouds in the arctic. *Proceedings of the National Academy of Sciences*, **118 (13)**, e2021387 118, https://doi.org/10.1073/pnas.2021387118, URL https://www.pnas.org/doi/abs/10.1073/pnas.2021387118, https://www.pnas.org/doi/pdf/10.1073/pnas.2021387118.

McFarquhar, G. M., G. Zhang, M. R. Poellot, G. L. Kok, R. McCoy, T. Tooman, A. Fridlind, and A. J. Heymsfield, 2007: Ice properties of single-layer stratocumulus during the Mixed-Phase Arctic Cloud Experiment: 1. observations. *J. Geophys. Res.*, **112 (D24201)**, https://doi.org/10.1029/2007JD008633.

Mossop, S. C., and J. Hallett, 1974: Ice crystal concentration in cumulus clouds: Influence of the drop spectrum. *Science*, **186 (4164)**, 632–634, https://doi.org/10.1126/science.186.4164.632, URL https://www.science.org/doi/abs/10.1126/science.186.4164.632, https://www.science.org/doi/pdf/10.1126/science.186.4164.632.

Murray, B. J., D. O'Sullivan, J. D. Atkinson, and M. E. Webb, 2012: Ice nucleation by particles immersed in supercooled cloud droplets. *Chem. Soc. Rev.*, **41**, 6519–6554, https://doi.org/10.1039/C2CS35200A, URL http://dx.doi.org/10.1039/C2CS35200A.

Pasquier, J. T., and Coauthors, 2022: Conditions favorable for secondary ice production in arctic mixed-phase clouds. *Atmospheric Chemistry and Physics Discussions*, **2022**, 1–33, https://doi.org/10.5194/acp-2022-314, URL https://acp.copernicus.org/preprints/acp-2022-314/.

Phillips, V. T. J., S. Patade, J. Gutierrez, and A. Bansemer, 2018: Secondary ice production by fragmentation of freezing drops: Formulation and theory. *Journal of the Atmospheric Sciences*, **75 (9)**, 3031 – 3070, https://doi.org/10.1175/JAS-D-17-0190.1, URL https://journals.ametsoc.org/view/journals/atsc/75/9/jas-d-17-0190.1.xml.

Phillips, V. T. J., J.-I. Yano, and A. Khain, 2017: Ice multiplication by breakup in ice–ice collisions. part i: Theoretical formulation. *Journal of the Atmospheric Sciences*, **74 (6)**, 1705 – 1719, https://doi.org/10.1175/JAS-D-16-0224.1, URL https://journals.ametsoc.org/view/journals/atsc/74/6/jas-d-16-0224.1.xml.

Prenni, A. J., and Coauthors, 2007: Can ice-nucleating aerosols affect arctic seasonal climate? *Bull. Amer. Meteor. Soc.*, **88**, 541–550.

Rangno, A. L., and P. V. Hobbs, 2001: Ice particles in stratiform clouds in the arctic and possible mechanisms for the production of high ice concentrations. *Journal of Geophysical Research: Atmospheres*, **106 (D14)**, 15 065–15 075, https://doi.org/https://doi.org/10.1029/2000JD900286, URL https://agupubs.onlinelibrary.wiley.com/doi/abs/10.1029/2000JD900286, https://agupubs.onlinelibrary.wiley.com/doi/pdf/10.1029/2000JD900286.

Schemann, V., and K. Ebell, 2020: Simulation of mixed-phase clouds with the icon large-eddy model in the complex arctic environment around ny-Ålesund. *Atmospheric Chemistry and Physics*, **20 (1)**, 475–485, https://doi.org/10.5194/acp-20-475-2020, URL https://acp.copernicus.org/articles/20/475/2020/.

Schwarzenboeck, A., V. Shcherbakov, R. Lefevre, J.-F. Gayet, Y. Pointin, and C. Duroure, 2009: Indications for stellar-crystal fragmentation in arctic clouds. *Atmospheric Research*, **92 (2)**, 220–228, https://doi.org/https://doi.org/10.1016/j.atmosres.2008.10.002, URL https://www.sciencedirect.com/science/article/pii/S0169809508002792.

Seifert, A., and K. D. Beheng, 2006: A two-moment cloud microphysics parameterization for mixed-phase clouds. Part 1: Model description. *Meteorol. Atmos. Phys.*, **92**, 45–66.

Shupe, M. D., S. Y. Matrosov, and T. Uttal, 2006: Arctic mixed-phase cloud properties derived from surface-based sensors at SHEBA. *J. Atmos. Sci.*, **63**, 697–711.

Solomon, A., G. Feingold, and M. D. Shupe, 2015: The role of ice nuclei recycling in the maintenance of cloud ice in Arctic mixed-phase stratocumulus. *Atmos. Chem. Phys.*, **15**, 10 631–10 643.

Sotiropoulou, G., L. Ickes, A. Nenes, and A. M. L. Ekman, 2021a: Ice multiplication from ice–ice collisions in the high arctic: sensitivity to ice habit, rimed fraction, ice type and uncertainties in the numerical description of the process. *Atmospheric Chemistry and Physics*, **21 (12)**, 9741–9760, https://doi.org/10.5194/acp-21-9741-2021, URL https://acp.copernicus.org/articles/21/9741/2021/.

Sotiropoulou, G., S. Sullivan, J. Savre, G. Lloyd, T. Lachlan-Cope, A. M. L. Ekman, and A. Nenes, 2020: The impact of secondary ice production on arctic stratocumulus. *Atmospheric Chemistry and Physics*, **20 (3)**, 1301–1316, https://doi.org/10.5194/acp-20-1301-2020, URL https://acp.copernicus.org/articles/20/1301/2020/.

Sotiropoulou, G., E. Vignon, G. Young, H. Morrison, S. J. O'Shea, T. Lachlan-Cope, A. Berne, and A. Nenes, 2021b: Secondary ice production in summer clouds over the antarctic coast: an underappreciated process in atmospheric models. *Atmospheric Chemistry and Physics*, **21 (2)**, 755–771, https://doi.org/10.5194/acp-21-755-2021, URL https://acp.copernicus.org/articles/21/755/2021/.

Sullivan, S. C., C. Hoose, A. Kiselev, T. Leisner, and A. Nenes, 2018: Initiation of secondary ice production in clouds. *Atmospheric Chemistry and Physics*, **18 (3)**, 1593–1610, https://doi.org/10.5194/acp-18-1593-2018, URL https://acp.copernicus.org/articles/18/1593/2018/.

Tornow, F., A. S. Ackerman, and A. M. Fridlind, 2021: Preconditioning of overcast-to-broken cloud transitions by riming in marine cold air outbreaks. *Atmospheric Chemistry and Physics*, **21 (15)**, 12 049–12 067, https://doi.org/10.5194/acp-21-12049-2021, URL https://acp.copernicus.org/articles/21/12049/2021/.

Turner, D. D., S. A. Clough, J. C. Liljegren, E. E. Clothiaux, K. E. Cady-Pereira, and K. L. Gaustad, 2007: Retrieving liquid water path and precipitable water vapor from Atmospheric Radiation Measurement (ARM) microwave radiometers. *IEEE Trans. Geosci. Remote Sensing*, **45**, 3680–3690.

Vergara-Temprado, J., and Coauthors, 2018: Strong control of Southern Ocean cloud reflectivity by ice-nucleating particles. *Proceedings of the National Academy of Sciences of the United States of America*, **115 (11)**, 2687–2692, https://doi.org/10.1073/pnas.1721627115.

Verlinde, J., and Coauthors, 2007: The Mixed-Phase Arctic Cloud Experiment. *Bull. Amer. Meteor. Soc.*, **88**, 205–221, https://doi.org/10.1175/BAMS-88-2-205.

Wegener, A., 1911: *Thermodynamik der Atmosphäre*. Leipzig, J. A. Barth, 1911.

Zhao, X., X. Liu, V. T. J. Phillips, and S. Patade, 2021: Impacts of secondary ice production on arctic mixed-phase clouds based on arm observations and cam6 single-column model simulations. *Atmospheric Chemistry and Physics*, **21 (7)**, 5685–5703, https://doi.org/10.5194/acp-21-5685-2021, URL https://acp.copernicus.org/articles/21/5685/2021/.

Zängl, G., D. Reinert, P. Rípodas, and M. Baldauf, 2015: The icon (icosahedral non-hydrostatic) modelling framework of dwd and mpi-m: Description of the non-hydrostatic dynamical core. *Quarterly Journal of the Royal Meteorological Society*, **141 (687)**, 563–579, https://doi.org/https://doi.org/10.1002/qj.2378, URL https://rmets.onlinelibrary.wiley.com/doi/abs/10.1002/qj.2378, https://rmets.onlinelibrary.wiley.com/doi/pdf/10.1002/qj.2378.